nature medicine

Time-lapse imaging of disease progression in deep brain areas using fluorescence microendoscopy

Robert P J Barretto[1,6], Tony H Ko[1,6], Juergen C Jung[1,6], Tammy J Wang[1], George Capps[1], Allison C Waters[1], Yaniv Ziv[1], Alessio Attardo[1], Lawrence Recht[2,3] & Mark J Schnitzer[1,4,5]

The combination of intravital microscopy and animal models of disease has propelled studies of disease mechanisms and treatments. However, many disorders afflict tissues inaccessible to light microscopy in live subjects. Here we introduce cellular-level time-lapse imaging deep within the live mammalian brain by one- and two-photon fluorescence microendoscopy over multiple weeks. Bilateral imaging sites allowed longitudinal comparisons within individual subjects, including of normal and diseased tissues. Using this approach, we tracked CA1 hippocampal pyramidal neuron dendrites in adult mice, revealing these dendrites' extreme stability and rare examples of their structural alterations. To illustrate disease studies, we tracked deep lying gliomas by observing tumor growth, visualizing three-dimensional vasculature structure and determining microcirculatory speeds. Average erythrocyte speeds in gliomas declined markedly as the disease advanced, notwithstanding significant increases in capillary diameters. Time-lapse microendoscopy will be applicable to studies of numerous disorders, including neurovascular, neurological, cancerous and trauma-induced conditions.

Chronic animal preparations that permit time-lapse intravital microscopy have allowed longitudinal imaging studies of disease models and have yielded insights regarding disease mechanisms and therapeutic strategies[1]. In neuroscience, time-lapse microscopy studies[2–5] have examined disease and injury in the peripheral nervous system[6,7] and superficial neocortex[1,8–11]. Although many pathologies afflict deeper brain structures, limited penetration of light into tissue precludes intravital microscopy in deep areas[1] such as the hippocampus or striatum. To overcome this, we developed time-lapse capabilities for *in vivo* microendoscopy[12,13] allowing repeated observations over weeks in deep brain areas.

Microendoscopy enables cellular imaging beneath the penetration depth of conventional light microscopy[14], relying on microlenses to provide micron-scale resolution during direct insertion into tissue[12,13,15]. Contrast modalities compatible with microendoscopy include wide-field epifluorescence as well as laser-scanning confocal, two-photon fluorescence, and second-harmonic generation fluorescence[14]. The use of these modalities, including in humans[16,17], has enabled cellular imaging in the cochlea, hippocampus, thalamus, deep neocortex, digestive tract and muscles, albeit only in acute studies[14].

Here we introduce time-lapse microendoscopy and illustrate its applicability to studies of brain disease. We developed a mouse preparation permitting repeated one- and two-photon fluorescence imaging by insertion of micro-optical probes into surgically implanted guide tubes. These two modalities respectively enabled high-speed (100–1,200 Hz) and three-dimensional imaging at the same tissue sites. We mainly studied hippocampus but in some mice examined striatum.

In adult mice expressing fluorescent proteins in a subset of CA1 hippocampal neurons[18], time-lapse microendoscopy allowed us to test the hypothesis that these neurons gradually change their dendritic branching patterns. This hypothesis is contrary to results from neocortical pyramidal cells[5,19,20], but CA1 receives disynaptic input from the dentate gyrus, where new neurons are continually added throughout adulthood[21]. It has been unknown whether circuits downstream from the dentate gyrus undergo a consequent remodeling, and we expected to see such an effect. Instead, the data revealed marked stability of CA1 neurons' dendritic structure, raising questions about how circuits downstream of the dentate gyrus accommodate continual addition of new inputs.

To illustrate the applicability to disease studies, we examined a mouse model of glioma, the most common primary malignant brain tumor. For poorly understood reasons, glioma growth depends on anatomical location. Primary gliomas arise preferentially in deep brain structures, and location correlates with tumor phenotype[22–24]. Studies in rats have suggested specific deep regions associate with the highest rates of glioma growth[25]. Thus, the local microenvironment, including concentrations of angiogenic factors, is thought to be a major influence on tumor enlargement[26]. Intravital microscopy studies of glioma angiogenesis have involved tumor implantation into the superficial neocortex, outside normal sites of primary incidence[27,28]. Time-lapse microendoscopy allowed us to observe glioma angiogenesis in an orthotopic, deep position in the brain and to track hallmark features, including vessel sizes and flow speeds.

Our experimental design, in which each mouse yields data from both normal tissue and a tumor at the bilaterally symmetric location,

[1]James H. Clark Center for Biomedical Engineering & Sciences, Stanford University, Stanford, California, USA. [2]Department of Neurology and Neurological Sciences, Stanford University, Stanford, California, USA. [3]Department of Neurosurgery, Stanford University, Stanford, California, USA. [4]Howard Hughes Medical Institute, Stanford University, Stanford, California, USA. [5]CNC Program, Stanford University, Stanford, California, USA. [6]These authors contributed equally to this work. Correspondence should be sent to M.J.S. (mschnitz@stanford.edu).

Received 5 November 2009; accepted 7 October 2010; published online 16 January 2011; doi:10.1038/nm.2292

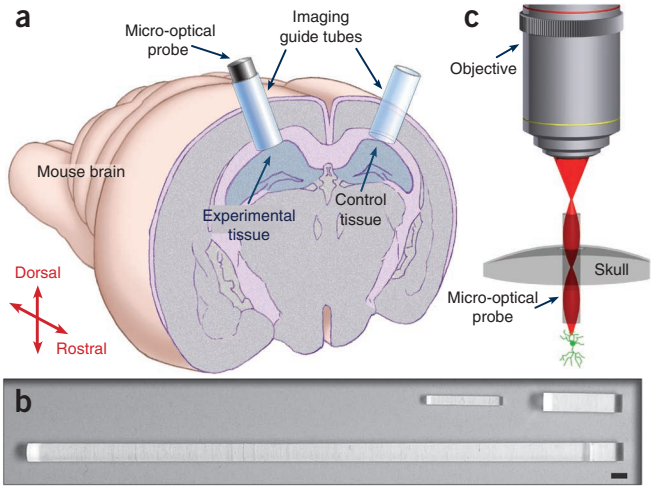

Figure 1 Chronic mouse preparation for repeated imaging of deep brain tissues using microendoscopy. (**a**) The experiment begins with implantation of imaging guide tubes, one into each hemisphere of the mouse's brain. After the mouse recovers from surgery, micro-optical probes can be repeatedly inserted into the guide tubes to allow time-lapse imaging. (**b**) Three microendoscope probes, a 500-µm-diameter singlet, a 1-mm-diameter singlet and a 1-mm-diameter compound doublet. Scale bar, 1 mm. (**c**) Schematic of a microscope objective lens coupling illumination into a 500-µm-diameter singlet microendoscope probe, such as that shown in **b**.

separates putative effects of the methodology from the disease. We performed >15,000 determinations of vessel diameters and flow speeds. The data show that the basic angiogenic dynamics seen in superficial tissues[26] are not specific to those areas and reveal the kinetics with which vascular morphology and flow speeds evolve during glioma progression. This prompts future microendoscopy studies of how and why tumor dynamics vary across brain areas.

RESULTS

Chronic preparation for time-lapse microendoscopy

We developed a mouse preparation for repeated imaging of deep brain tissue (**Fig. 1**). Implantation into the brain of one or two (bilateral) guide tubes allowed repeated insertion of microendoscopes to the same sites (**Fig. 1a**). Each guide tube comprised a glass capillary with a glass window at the tip, allowing optical but not physical access to tissue. In size, the microendoscopes (500- and 1,000-µm lens diameters) resemble microdialysis probes more than microelectrodes (**Fig. 1b**), so the capillaries had to be appropriately placed to minimize mechanical perturbation to the imaged tissue.

We achieved this by placing the guide tubes' tips just dorsal to, but not within, the brain structure of interest. Neither the guide tubes nor the microendoscopes entered the tissue being studied, instead allowing imaging from nearby. Most of our studies were of hippocampus, with guide tubes just dorsal to the CA1 hippocampal area, allowing our microendoscopes to inspect CA1 (**Fig. 1a**). For imaging striatum the guide tubes resided just dorsal to this structure.

After allowing the mice to recover from surgery, we performed microendoscopy repeatedly over periods regularly lasting 7 weeks, but in a few mice >1 year. To initiate imaging, we inserted a micro-optical probe into a mouse's guide tube, and we placed the mouse on the stage of an upright microscope modified to accommodate microendoscopy[13,15]. The microscope objective lens focused illumination near the top face of the micro-optical probe, which refocused the illumination into the brain (**Fig. 1c**). These probes were generally compound doublet gradient refractive index (GRIN) microlenses, composed of an objective (0.49 numerical aperture) and a relay lens (0.2 numerical aperture), or single GRIN microlenses (0.45–0.48 numerical aperture) (**Fig. 1b**). A snug fit between the probe and guide tube facilitated multiple returns to the same tissue for one- and two-photon microendoscopy. Focal adjustment of the microscope objective lens altered the focus in tissue[12,13,15]. This enabled three-dimensional sectioning by two-photon microendoscopy, in some cases up to ~650 µm from the tip of the guide tube (**Supplementary Video 1**). This optical penetration is much further than reported for acute microendoscopy[12,13] and nearly comparable to depths (~600–700 µm) achievable by conventional two-photon microscopy[29].

As with any foreign entity implanted into the brain—including electrodes, microdialysis probes or cranial windows—we expected glial activation surrounding the implanted guide tubes. Post-mortem tissue examinations near our guide tubes confirmed this, revealing a thin (~25–40-µm) tissue layer showing greater labeling by antibodies specific for glial fibrillary acidic protein as compared to adjacent tissue (**Supplementary Fig. 1a–e**). These specimens revealed no loss of neurons beneath the guide tubes, as compared to contralateral hippocampal areas in the same mice ($P < 1 \times 10^{-5}$; one-tailed Wilcoxon signed-rank test; $n = 3$ mice, 2,098 cells). Given the optical penetration of up to ~650 µm, the glial activation layer did not obstruct the imaging of tissue lying well beyond. This is consistent with reports describing microscopy through cranial windows, which cause similar levels of gliosis[30]. The main implication is that microendoscopy studies of disease must control for the potential side effects of guide tube implantation to separate them from the effects of disease.

Repeated imaging of neurons and microvasculature

Before studying disease, we assessed our method's basic capabilities and found it possible to track individual neurons, dendrites and cerebral microvasculature over weeks.

In mice expressing yellow or green fluorescent protein (YFP or GFP) in sparse subsets of CA1 pyramidal neurons[18], we monitored neurons and dendrites (**Fig. 2**). Three-dimensional data from two-photon microendoscopy facilitated inspection of dendritic morphologies up to ~530 µm from the dorsal CA1 surface (**Fig. 2b,c**). This covers all of hippocampal layers stratum oriens and stratum pyramidale, where pyramidal neurons have their basal dendrites and somata, respectively, and midway into stratum radiatum, where these cells' apical dendrites lie.

Whether dendritic branching patterns of adult hippocampal pyramidal neurons are plastic or stable has remained unanswered owing to the lack of suitable imaging techniques. Unlike in acute imaging studies of hippocampus[13,31], we repeatedly inspected dendritic branching patterns over weeks (**Fig. 2a–c**). We analyzed images of 4,257 dendrites, tracked via a total 33,596 dendrite observations over 7 weeks in ten mice (**Supplementary Methods**). The data revealed only 16 instances of dendrite turnover (**Supplementary Fig. 2**), defined as the dendrite either showing a new segment or a segment disappearing from view. This yielded an estimate of $<0.00013 \pm 0.00003$ (mean ± s.e.m.; $n = 33{,}596$ observations) for the probability per day of an individual dendrite undergoing a turnover event. This rate of change should be regarded as an upper bound and, under a simplifying assumption of a uniform rate, corresponds to an estimated lower bound of 8,000 ± 2,000 d for the mean stability lifetime of a dendrite, longer than a mouse's lifetime. Investigations of how this stability might be altered in the diseased hippocampus represent important future studies.

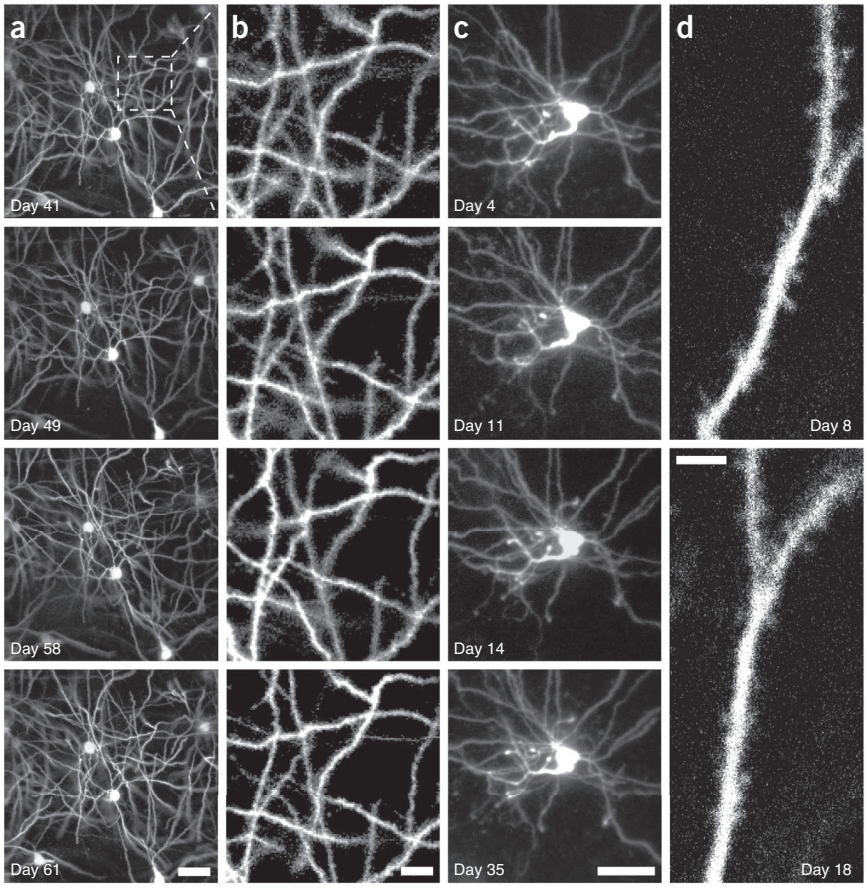

Figure 2 Time-lapse two-photon microendoscopy of CA1 hippocampal neurons. Time-lapse image sequences of CA1 pyramidal neurons in three *Thy1-GFP* mice. (**a**,**b**) Two-dimensional projections of three-dimensional stacks containing four image slices acquired at 4.2-µm axial spacing over 16.8 µm in depth. **b** shows enlargements of the boxed area in **a**. (**c**) Two-dimensional projections of three-dimensional stacks acquired at 3-µm axial spacing over approximately 540 µm in depth. (**d**) Enlarged, single-image frames revealing spiny dendrites. Scale bars in **a**, **b**, **c** and **d** are 100, 25, 50 and 5 µm, respectively.

In wild-type mice, three-dimensional imaging enabled examination of vascular networks in hippocampus (**Fig. 3a** and **Supplementary Video 1**) and striatum (**Supplementary Fig. 3**), which were revealed up to over ~650 µm depths following intravascular injection of fluorescein-dextran dye. After structural imaging by two-photon microendoscopy, we could switch immediately to high-speed (100–1,200 Hz) imaging of erythrocyte flow by one-photon microendoscopy (**Fig. 3**). Single erythrocytes were generally apparent, appearing in relief against the dye-labeled blood plasma (**Supplementary Video 2**). Computational analysis extracted structural parameters, such as vessel diameters, and physiological parameters, such as flow speeds (**Supplementary Fig. 4**). Such time-lapse monitoring of cerebrovascular properties should also be applicable to studies of stroke or neurodegenerative diseases.

Time-lapse imaging of glioma angiogenesis

To illustrate studies of disease, we examined a mouse model of glioma. We implanted two guide tubes at bilaterally symmetric sites, dorsal to left and right CA1 areas (**Fig. 1a**). We inoculated the right site with GL261 mouse glioma cells; the left site received no glioma cells and served as a control. This enabled control and experimental data to be acquired from each mouse, yielding matched sets in regard to subjects' ages, sexes and life histories.

Using time-lapse microendoscopy, we were generally able to track imaging sites over the entire disease time course, ~22–24 d in total from glioma inoculation to subject mortality. We also

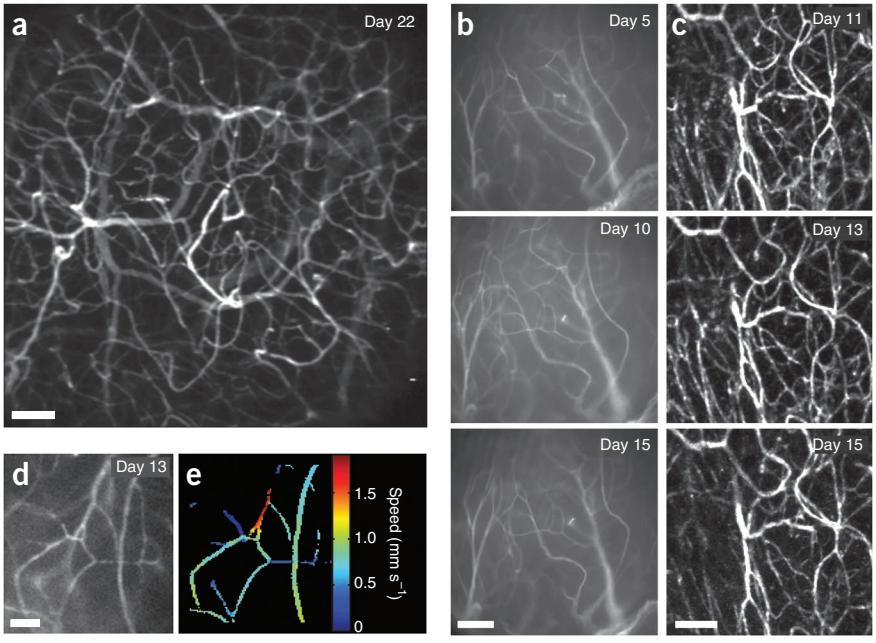

Figure 3 Time-lapse microendoscopy of CA1 microvasculature shows normal blood vessel morphologies are stable over time. (**a**) Two-dimensional projection of a three-dimensional stack of 220 images of dye-labeled vasculature acquired at ~3-µm increments over ~660 µm in depth. **Supplementary Video 1** shows the entire image stack. (**b**) Time-lapse image sequence acquired by one-photon microendoscopy. (**c**) Time-lapse sequence of two-photon image stacks, each composed of 40–50 images acquired approximately 3.7 µm apart in depth and projected to two dimensions. **Figure 4b** shows dye-labeled tumor vessels from the opposing (experimental) hippocampus in the same mouse. (**d**,**e**) One-photon image of CA1 blood vessels (**d**) and corresponding microcirculatory speed map (**e**), determined by high-speed (100-Hz) imaging and cross-correlation analysis. **Supplementary Video 2** shows blood flow from this same field of view. Scale bars are 100 µm in **a**–**c** and 50 µm in **d**.

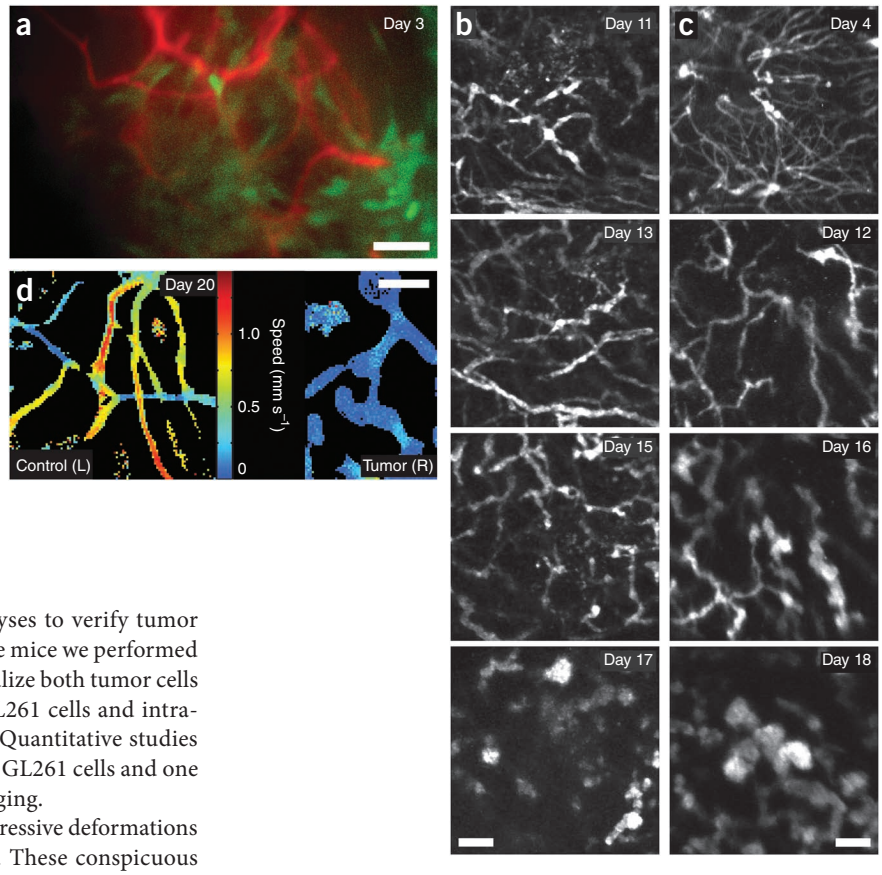

Figure 4 Time-lapse imaging of glioma angiogenesis in mouse CA1 reveals progressive distortions to vascular geometry and reduced microcirculatory speeds. (**a**) Dual-color image of GFP-expressing mouse glioma cells (green) and rhodamine-dextran–labeled microvasculature (red), acquired in a live mouse by one-photon fluorescence microendoscopy on day 3 after glioma cell inoculation. (**b**,**c**) Time-lapse sequences of two-photon microendoscopy image stacks, projected to two dimensions, showing the progressive distortion of the microvasculature due to glioma angiogenesis. Each stack contained 40–50 images acquired 3.7 µm apart in depth. **Figure 3c** shows images of the opposing (control) hippocampus from the same mouse used in **b**. (**d**) Maps of average erythrocyte speed, determined from 10-s videos acquired at 100 Hz by one-photon microendoscopy, in left (control) and right (experimental) hemispheres of a live mouse on day 20 after glioma inoculation. Scale bars, 100 µm.

performed postmortem histopathological analyses to verify tumor invasiveness (**Supplementary Fig. 1f**,**g**). In some mice we performed dual-color microendoscopy, allowing us to visualize both tumor cells and blood vessels by using GFP-transfected GL261 cells and intravascular injection of rhodamine dye (**Fig. 4a**). Quantitative studies of angiogenic dynamics relied on untransfected GL261 cells and one fluorescence channel dedicated to vascular imaging.

Over the weeks of glioma growth, we saw progressive deformations and size increases of tumor vessels (**Fig. 4b**,**c**). These conspicuous changes (**Fig. 4b**) did not occur at control sites in the same mice (**Fig. 3c**). In early disease stages (days 1–5), tumor vessels showed distortions from normal shapes (**Fig. 4c**). At intermediate stages (days 6–15), tumor vessels increased in diameter and vascular distortions worsened (**Supplementary Video 3**). By late stages (days 16–24), many tumor vessels appeared thrombotic, and blood flow dropped noticeably in tumors but not normal tissue (**Fig. 4b–d**).

Quantitative analysis of angiogenesis

We quantified changes in vessel morphology and flow speeds by analyses of the three-dimensional and high-speed imaging data sets, respectively (**Figs. 3e**, **4d**, **5** and **Supplementary Fig. 4**; **Supplementary Methods**). Individual mice showed considerable day-to-day and between-subject variations but generally reflected findings made from the aggregated population data. Throughout glioma progression, mean vessel diameters in normal tissue remained constant ($P = 0.23$; Kruskal-Wallis analysis of variance) and were 12.6 ± 1.7 µm (grand mean ± s.d.; $n = 7$ mice; 2,830 diameter measurements aggregated over all days) (**Fig. 5a**,**b**). Not surprisingly, erythrocyte flow speeds in normal tissue (389 ± 191 µm s^{-1}; $n = 10$ mice; 8,060 speed measurements over all days) fluctuated more day to day than did vessel diameters but showed no significant changes across the experiment's duration ($P = 0.06$) (**Fig. 5a**,**b**).

By comparison, progressive increases in vessel diameter and decreases in flow speed at glioma sites were significant ($P = 0.009$ and $P = 0.01$, respectively; Kruskal-Wallis analysis of variance). Aggregated measurements of diameter (17.0 ± 5.3 µm; $n = 7$ mice; 1,695 measurements over all days) and speed (134 ± 112 µm s^{-1}; $n = 10$ mice; 5,822 measurements) from glioma also differed significantly

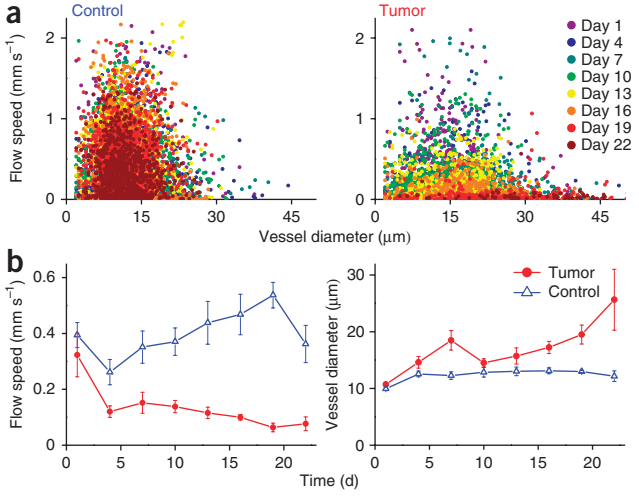

Figure 5 Quantitative tracking of glioma angiogenesis in CA1 hippocampus shows tumor vessels broaden in diameter but undergo marked declines in flow speed. Vessel diameters and erythrocyte flow speeds were monitored as a function of elapsed time after an initial surgery and glioma cell implantation on day 0. Not all mice were imaged at identical time points, so time values were binned into 3-d intervals. (**a**) Plots of flow speed versus vessel diameter, for control tissue (left) and tumor sites (right), in which each data point represents an individual vessel segment. Unlike at control sites, at tumor sites the data reveal an overall progressive decrease in flow speeds and increase in vessel diameters as the disease advanced ($n = 10$ mice). (**b**) Population averages of erythrocyte flow speed (left) and vessel diameter (right) are plotted (mean ± s.e.m.) versus elapsed time. Mean tumor vessel diameters and flow speeds differed significantly from control values ($P < 1 \times 10^{-6}$ and $P < 1 \times 10^{-15}$, respectively; Mann-Whitney U test).

from normal tissue ($P < 10^{-6}$ and $P < 1 \times 10^{-15}$, respectively; Mann-Whitney U test). Significant differences in flow speed between normal and tumor sites appeared and were maintained from as early as day 7 ($P < 0.05$; Mann-Whitney U tests). Significant differences in vessel size were maintained from day 16 onwards ($P < 0.05$). Glioma also altered vascular network structure, as branching ratios (the ratios of vessels' total lengths to the number of branches) were lower at tumor sites (245 ± 103 µm per branch; mean ± s.d.; $n = 10$ mice) than in control tissue (403 ± 190 µm per branch) from day 13 onward ($P < 0.05$; Mann-Whitney U tests). Overall, our analyses showed that, as the disease progressed, mean flow speeds and branching ratios declined markedly in glioma, but not in normal tissue, despite an increase in average tumor vessel diameters (**Fig. 5b**). Plots of the vessels' speeds versus their diameters illustrated that, unlike at normal sites, at tumor sites the relationship between these variables showed conspicuous, progressive alterations (**Fig. 5a**). Thus, the basic features of glioma angiogenesis regarding reduced flow speed and distorted vasculature, previously identified in superficial brain tissues[26–28], also arise for gliomas in an orthotopic, deep-brain location.

DISCUSSION

We have introduced a means for cellular-level, time-lapse imaging of deep brain structures. We focused on the hippocampus, but our methodology is not specific to this area, as illustrated in striatum (**Supplementary Fig. 3**). Our approach draws on the long experience in neuroscience with implantation of similarly sized guide tubes for microdialysis and electrophysiological recordings and should be broadly applicable. The imaging depths attained here, up to ~650 µm from the guide tube, will facilitate studies of numerous disorders. Alternatively, one might implant micro-optical probes directly into the brain without guide tubes. However, guide tubes permit individual micro-optical probes to be used across many animals and allow inspection of one tissue site with multiple probes of different optical designs.

A key advantage of our approach over histological approaches concerns the experimental designs that can be achieved by longitudinal studies, as compared to those in which tissue culture specimens are taken from different cohorts of animals at distinct time points[1]. The benefits of longitudinal imaging include a substantial reduction in the number of experimental animals needed, as each animal ideally provides data at all time points. Moreover, longitudinal imaging yields dynamic information from individual animals, which is often pivotal for disease studies by revealing how early symptoms correlate with later disease outcomes or might be reversed by intervention. As illustrated by our observations of hippocampal dendrites, tracking individual cells avoids the confound of cell-to-cell variations in the analysis of temporal dynamics. The ability to monitor dendrites should be particularly useful for studying developmental[32], neurodegenerative[8], cerebrovascular[33] and epileptic[34] disorders that affect dendritic structures. The capacity to monitor striatum should aid the study of several prevalent motor and addictive disorders.

Although time-lapse microendoscopy opens new experimental possibilities, researchers should also appreciate the limitations. Guide tube implantation necessarily perturbs the brain. We minimized the impact by placing guide tubes outside, not within, the tissue being imaged. Implanting a microendoscope with a microprism for sideways viewing of tissue adjacent to the insertion path[35] or advancing a microendoscope over days, akin to how electrodes are often implanted, may be viable alternatives. Our basic approach induced a ~25–40-µm layer of glial activation surrounding the implant. As with implanted cranial windows for intravital microscopy[30], glial activation generally declined over time and permitted imaging well beyond the activated layer.

Nevertheless, researchers must design disease studies that separate the effects of experimental procedures from those of the disease. A recent debate on the relative merits of the thinned-skull versus cranial-window preparations for intravital microscopy studies arose in a context that did not easily permit comparisons between control and experimentally manipulated subjects[30]. By contrast, observable effects of many brain diseases are profound, as shown here for glioma, and images from control and tumor sites were typically distinguishable at a glance.

CA1 pyramidal neurons support spatial and episodic memory, but the long-term stability of hippocampal dendrites had not previously been assessed. Analyses of dendrite stability in neocortical pyramidal neurons have been based on data from ~50–125 dendrites[5,19,20] and imply bounds on dendrite turnover of <0.5–0.8% over ~1–2 months. We tracked >4,200 dendrites over 7 weeks to test the hypothesis that CA1 pyramidal neurons undergo gradual changes in dendrite structure under normal conditions. Our data provided little support for this idea. The 16 turnover events we saw imply an upper bound on turnover of <0.4%, comparable to or less than that for neocortical neurons. This establishes baseline stability levels against which studies of disease models or aged animals can be compared and indicates that individual dendritic segments of CA1 pyramidal neurons have an estimated mean lifetime of >8,000 ± 2,000 d. These neurons each have ~200 dendritic segments[36], suggesting individual neurons might undergo a major dendritic change every >40 d. Under a simplifying assumption of a uniform rate of alteration, <4% of dendritic segments would change over a year. Thus, we cannot rule out dendritic turnover, but the extremely few instances we saw are just above the estimated reliability limits of our scoring procedures (**Supplementary Methods**). We studied healthy mice housed in standard conditions, and it will be interesting to test whether manipulations that increase hippocampal plasticity, such as environmental enrichment, promote dendritic plasticity above the rates reported here.

Glioma is the most common primary intracranial tumor in humans[37]. As glioma preferentially strikes deep brain locations[22–24], it has been challenging to study the angiogenic dynamics in orthotopic models. Using time-lapse microendoscopy, we tracked angiogenesis in deep tumors over weeks. The GL261 glioma cells we used possess the main characteristics of most glioma models, including invasive but nonmetastatic growth[38]. By monitoring flow speeds, vessel diameters, and relationships between the two, we found tumor vessels show progressive decreases in flow speed despite more than doubling in mean diameter (**Fig. 5**). The basic dynamical features of angiogenesis seen by intravital microscopy are thus not specific to superficial tissues. Microendoscopy should facilitate comparisons of angiogenesis between different brain locations and tumor lines with distinct angiogenic characteristics[11]. Implantation of multiple guide tubes per animal should allow within-subject comparisons between different locally applied treatments.

Overall, time-lapse microendoscopy should broadly enable studies of brain disorders such as cerebrovascular, neurodegenerative, epileptic and trauma-induced conditions that have eluded examination in deep tissues by light microscopy[1]. There are already a large set of fluorescent markers of pertinence to disease studies, such as labels for amyloid plaques[10], reactive oxygen species[9] and glia and immune cells[1], and many of these should be readily usable in combination with microendoscopy. Miniaturized microscopes based on micro-optics allow deep tissue imaging in behaving mice[39], suggesting the feasibility of time-lapse studies in which cellular and behavioral effects of disease are visualized simultaneously.

METHODS

Methods and any associated references are available in the online version of the paper at http://www.nature.com/naturemedicine/.

Note: Supplementary information is available on the Nature Medicine website.

ACKNOWLEDGMENTS

This work was initiated under National Institute on Drug Abuse CEBRA DA017895 and further supported by National Institute of Neurological Disorders and Stroke R01NS050533, National Cancer Institute P50CA114747 and a research contract with Mauna Kea Technologies. We gratefully acknowledge support from the Stanford–US National Institutes of Health Biophysics Program (R.P.J.B.) and a Machiah postdoctoral fellowship (Y.Z.). We thank M. Lim and J. Weimann for help with GL261 cells, S. Kim, T. Jang, A. Lui, J. Li and M. Ramkumar for technical assistance with histology and image processing, E. Mukamel for helpful conversations and B. Colyear and B. Wilt for help with graphic illustration.

AUTHOR CONTRIBUTIONS

R.P.J.B. designed experiments, developed tracking of neuronal dendrites, performed the study on CA1 neuron stability, analyzed the neuronal histology data, validated the algorithm for computing erythrocyte speeds and computed relationships between vessel diameters and speeds. T.H.K. designed experiments, performed the glioma experiments and computed flow speeds and vessel sizes. J.C.J. designed experiments, developed the chronic preparation and tested it for imaging neurons and gliomas. T.J.W. and G.C. performed neuronal imaging and contributed to the glioma experiments. A.C.W. developed bilateral imaging, performed neuronal imaging and contributed to the glioma experiments. Y.Z. developed and performed striatal imaging. A.A. performed histological analyses and analyzed vessel branching ratios. L.R. designed experiments and supervised the glioma study. M.J.S. designed experiments, performed statistical testing, initiated and supervised the project and wrote the paper. All authors edited the paper.

COMPETING FINANCIAL INTERESTS

The authors declare competing financial interests: details accompany the full-text HTML version of the paper at http://www.nature.com/naturemedicine/.

Published online at http://www.nature.com/naturemedicine/.
Reprints and permissions information is available online at http://npg.nature.com/reprintsandpermissions/.

1. Misgeld, T. & Kerschensteiner, M. *In vivo* imaging of the diseased nervous system. *Nat. Rev. Neurosci.* **7**, 449–463 (2006).
2. Melder, R.J., Salehi, H.A. & Jain, R.K. Interaction of activated natural killer cells with normal and tumor vessels in cranial windows in mice. *Microvasc. Res.* **50**, 35–44 (1995).
3. Lichtman, J.W., Magrassi, L. & Purves, D. Visualization of neuromuscular junctions over periods of several months in living mice. *J. Neurosci.* **7**, 1215–1222 (1987).
4. Grutzendler, J., Kasthuri, N. & Gan, W.B. Long-term dendritic spine stability in the adult cortex. *Nature* **420**, 812–816 (2002).
5. Trachtenberg, J.T. *et al.* Long-term *in vivo* imaging of experience-dependent synaptic plasticity in adult cortex. *Nature* **420**, 788–794 (2002).
6. Kerschensteiner, M., Schwab, M.E., Lichtman, J.W. & Misgeld, T. *In vivo* imaging of axonal degeneration and regeneration in the injured spinal cord. *Nat. Med.* **11**, 572–577 (2005).
7. Bareyre, F.M., Kerschensteiner, M., Misgeld, T. & Sanes, J.R. Transgenic labeling of the corticospinal tract for monitoring axonal responses to spinal cord injury. *Nat. Med.* **11**, 1355–1360 (2005).
8. Tsai, J., Grutzendler, J., Duff, K. & Gan, W.B. Fibrillar amyloid deposition leads to local synaptic abnormalities and breakage of neuronal branches. *Nat. Neurosci.* **7**, 1181–1183 (2004).
9. McLellan, M.E., Kajdasz, S.T., Hyman, B.T. & Bacskai, B.J. *In vivo* imaging of reactive oxygen species specifically associated with thioflavine S–positive amyloid plaques by multiphoton microscopy. *J. Neurosci.* **23**, 2212–2217 (2003).
10. Meyer-Luehmann, M. *et al.* Rapid appearance and local toxicity of amyloid-β plaques in a mouse model of Alzheimer's disease. *Nature* **451**, 720–724 (2008).
11. Yuan, F. *et al.* Vascular permeability and microcirculation of gliomas and mammary carcinomas transplanted in rat and mouse cranial windows. *Cancer Res.* **54**, 4564–4568 (1994).
12. Levene, M.J., Dombeck, D.A., Kasischke, K.A., Molloy, R.P. & Webb, W.W. *In vivo* multiphoton microscopy of deep brain tissue. *J. Neurophysiol.* **91**, 1908–1912 (2004).
13. Jung, J.C., Mehta, A.D., Aksay, E., Stepnoski, R. & Schnitzer, M.J. *In vivo* mammalian brain imaging using one- and two-photon fluorescence microendoscopy. *J. Neurophysiol.* **92**, 3121–3133 (2004).
14. Flusberg, B.A. *et al.* Fiber-optic fluorescence imaging. *Nat. Methods* **2**, 941–950 (2005).
15. Jung, J.C. & Schnitzer, M.J. Multiphoton endoscopy. *Opt. Lett.* **28**, 902–904 (2003).
16. Hsiung, P.L. *et al.* Detection of colonic dysplasia *in vivo* using a targeted heptapeptide and confocal microendoscopy. *Nat. Med.* **14**, 454–458 (2008).
17. Llewellyn, M.E., Barretto, R.P., Delp, S.L. & Schnitzer, M.J. Minimally invasive high-speed imaging of sarcomere contractile dynamics in mice and humans. *Nature* **454**, 784–788 (2008).
18. Feng, G. *et al.* Imaging neuronal subsets in transgenic mice expressing multiple spectral variants of GFP. *Neuron* **28**, 41–51 (2000).
19. Lee, W.-C.A. Dynamic remodeling of dendritic arbors in GABAergic interneurons of adult visual cortex. *PLoS Biol.* **4**, 271–280 (2006).
20. Chow, D.K. *et al.* Laminar and compartmental regulation of dendritic growth in mature cortex. *Nat. Neurosci.* **12**, 116–118 (2009).
21. Li, Y., Mu, Y. & Gage, F.H. Development of neural circuits in the adult hippocampus. *Curr. Top. Dev. Biol.* **87**, 149–174 (2009).
22. Lim, D.A. *et al.* Relationship of glioblastoma multiforme to neural stem cell regions predicts invasive and multifocal tumor phenotype. *Neuro-oncol.* **9**, 424–429 (2007).
23. Larjavaara, S. *et al.* Incidence of gliomas by anatomic location. *Neuro-oncol.* **9**, 319–325 (2007).
24. Ramnarayan, R., Dodd, S., Das, K., Heidecke, V. & Rainov, N.G. Overall survival in patients with malignant glioma may be significantly longer with tumors located in deep grey matter. *J. Neurol. Sci.* **260**, 49–56 (2007).
25. Jang, T. *et al.* A distinct phenotypic change in gliomas at the time of magnetic resonance imaging detection. *J. Neurosurg.* **108**, 782–790 (2008).
26. Jain, R.K. *et al.* Angiogenesis in brain tumours. *Nat. Rev. Neurosci.* **8**, 610–622 (2007).
27. Kashiwagi, S. *et al.* Perivascular nitric oxide gradients normalize tumor vasculature. *Nat. Med.* **14**, 255–257 (2008).
28. Garkavtsev, I. *et al.* The candidate tumour suppressor protein ING4 regulates brain tumour growth and angiogenesis. *Nature* **428**, 328–332 (2004).
29. Helmchen, F. & Denk, W. Deep tissue two-photon microscopy. *Nat. Methods* **2**, 932–940 (2005).
30. Xu, H.T., Pan, F., Yang, G. & Gan, W.B. Choice of cranial window type for *in vivo* imaging affects dendritic spine turnover in the cortex. *Nat. Neurosci.* **10**, 549–551 (2007).
31. Mizrahi, A., Crowley, J.C., Shtoyerman, E. & Katz, L.C. High-resolution *in vivo* imaging of hippocampal dendrites and spines. *J. Neurosci.* **24**, 3147–3151 (2004).
32. Dierssen, M. & Ramakers, G.J. Dendritic pathology in mental retardation: from molecular genetics to neurobiology. *Genes Brain Behav.* **5**, Suppl 2, 48–60 (2006).
33. Li, P. & Murphy, T.H. Two-photon imaging during prolonged middle cerebral artery occlusion in mice reveals recovery of dendritic structure after reperfusion. *J. Neurosci.* **28**, 11970–11979 (2008).
34. Shapiro, L.A., Ribak, C.E. & Jessberger, S. Structural changes for adult-born dentate granule cells after status epilepticus. *Epilepsia* **49**, Suppl 5, 13–18 (2008).
35. Murayama, M., Perez-Garci, E., Luscher, H.R. & Larkum, M.E. Fiberoptic system for recording dendritic calcium signals in layer 5 neocortical pyramidal cells in freely moving rats. *J. Neurophysiol.* **98**, 1791–1805 (2007).
36. Pyapali, G.K., Sik, A., Penttonen, M., Buzsaki, G. & Turner, D.A. Dendritic properties of hippocampal CA1 pyramidal neurons in the rat: intracellular staining *in vivo* and *in vitro*. *J. Comp. Neurol.* **391**, 335–352 (1998).
37. Louis, D.N. Molecular pathology of malignant gliomas. *Annu. Rev. Pathol.* **1**, 97–117 (2006).
38. Szatmari, T. *et al.* Detailed characterization of the mouse glioma 261 tumor model for experimental glioblastoma therapy. *Cancer Sci.* **97**, 546–553 (2006).
39. Flusberg, B.A. *et al.* High-speed, miniaturized fluorescence microscopy in freely moving mice. *Nat. Methods* **5**, 935–938 (2008).

ONLINE METHODS

Mice. We used mice expressing fluorescent proteins driven by the *Thy1* promoter (YFP-H and GFP-M lines; 2–12 months of age) for neuronal imaging[18], but wild-type mice (BALB/c and C57BL/6 mice; 2–6 months of age) for glioma studies. All mouse experiments were approved by the Stanford Administrative Panel on Laboratory Animal Care.

Glioma cells. We used GL261 mouse glioma cells[38], maintained in Dulbecco's modified Eagle's medium supplemented with 10% fetal calf serum. In some studies, to visualize tumor progression via fluorescence we used a polyclonal mixture of GFP-transfected GL261 lines that were infected with amphotropic retrovirus containing a cytomegalovirus chick β-actin promoter driving GFP (created in house). We harvested glioma cells to a concentration of ~20,000 cells per μl.

Microlenses. For tumor imaging we generally used 1.0-mm-diameter GRIN lenses (0.48 numerical aperture, 0.45 pitch, 300 μm working distance in water) or 0.5-mm-diameter GRIN lenses (0.45 numerical aperture, 0.92 pitch, 300 μm working distance). For neuronal imaging, we also used 1-mm-diameter doublet microendoscopes with a 0.49 numerical aperture, 250 μm working distance, 0.218 pitch GRIN objective lens fused to a 1.75 pitch, 0.2 numerical aperture GRIN relay.

Guide tubes. For 1-mm-diameter microendoscopes, guide tube capillaries were 1.6-mm-inner-diameter, 1.8-mm-outer-diameter and 3 mm long; for 0.5-mm-diameter micro-optics, capillaries were 0.6-mm-inner-diameter, 0.84-mm-outer-diameter and 3 mm long. We cut and polished the capillaries and cleaned them by sonication. We then sealed them at one end with a cover slip (Gold Seal #0; cut to match the capillaries' outer dimensions) with ultraviolet-curing epoxy (Norland Optical Adhesive 81) to allow optical but not physical access to tissue. We fashioned washers (~500 μm thick) in silicone Elastosil RTV 625, cured them between two acrylic plates and placed one washer around each capillary. Alternatively, we made the washers in Kwik-Sil and diced them to size.

Surgery. We typically implanted two guide tubes at symmetric coordinates in opposing hemispheres (2.0 mm posterior to bregma, 2.0 mm lateral for hippocampus; 1.0 mm anterior to bregma, 1.8 mm lateral for striatum). We positioned the guide tube windows just dorsal to, but not within, CA1 hippocampus or dorsal striatum. The **Supplementary Methods** contain details.

Imaging sessions. We generally imaged mice for multiple 30–60-min sessions under anesthesia with isoflurane (1.5–2.5% in O_2) or intraperitoneal ketamine (75 mg per kg body weight) and xylazine (15 mg per kg body weight). We mounted the mice on a stereotaxic frame such that the capillary guide tube was parallel to the optical axis. We cleaned the capillary's inside to remove debris. We then inserted microendoscopes, matched to the inner capillary diameter, up to the guide tube window. Occasionally, we used a metal sheath fixed to the side of the microendoscope to aid repeatable positioning within the capillary. For glioma studies, we imaged mice every 2 or every 3 d, from days 1 to 24 after surgery. For neural imaging, in early studies we imaged mice at irregular intervals up to 396 d; in later studies used for quantitative analysis of dendrite turnover, we generally examined mice every 4 d over 7 weeks.

Optical instrumentation. Microendoscopy involved previously described instrumentation[13,15]. In brief, for one-photon microendoscopy we used a custom instrument with Hg-arc lamp illumination[13]. To deliver illumination into the microendoscopes, we used either a 10×, 0.25–numerical-aperture microscope objective (Zeiss, Achrostigmat) or a 20×, 0.40–numerical-aperture objective (Olympus, LMPlanFl) for the singlet microlenses and the 10×, –0.25 numerical-aperture objective (Zeiss, Achrostigmat) for the doublet microendoscopes. High-speed electron-multiplying charge-coupled device cameras captured videos of blood flow at frame rates up to 1.2 kHz, but typically 100 Hz. We used a Cascade 128 (Roper Scientific) camera and an iXon DU-897E (Andor) camera with the 1-mm- and 0.5-mm-diameter microendoscopes, respectively. A cooled charge-coupled device camera (Coolsnap HQ, Roper Scientific) captured higher-resolution images. In dual-color studies, a dichroic module (Dual-View, Optical Insights) projected two images in distinct colors onto one camera.

For two-photon microendoscopy we used a modified commercial two-photon microscope (Prairie Technologies) and a custom two-photon microscope[13,15], both adapted to accommodate the use of microendoscopy[17] and equipped with a tunable Ti:Sapphire laser (Mai-Tai, Spectra-Physics). The laser was tuned to 920 nm. We adjusted average power at the sample for consistency in signal strength across imaging sessions in each animal. Typical powers at the specimen surface were 5–18 mW, but always <25 mW. To couple illumination into the microendoscopes, we used a 10×, 0.25–numerical-aperture objective (Olympus, Plan N) in glioma studies or a 20×, 0.5–numerical-aperture objective (Carl Zeiss, EC Epiplan Neofluar) in striatal and CA1 dendrite stability studies. In a few sessions we used a 1-mm-diameter singlet GRIN microendoscope with an additional hemispheric lens at the tip[40], for increased numerical aperture and enhanced resolution over a reduced field of view (**Fig. 2d**).

Fluorescence angiography. To label the vasculature, we intravenously injected fluorescent dye (100–300 μl at 10 mg ml^{-1} concentration), either rhodamine-dextran (Molecular Probes; 70,000 molecular weight, neutral) or fluorescein-isothiocyanate dextran (Sigma-Aldrich FD2000S; 2,000,000 molecular weight), into the tail vein.

Analysis software. We performed image analysis using Matlab (MathWorks) and statistical analysis using Origin Pro (OriginLab). Details are in the **Supplementary Methods**.

Additional methods. Detailed methodology is described in the **Supplementary Methods**.

40. Barretto, R.P., Messerschmidt, B. & Schnitzer, M.J. *In vivo* fluorescence imaging with high-resolution microlenses. *Nat. Methods* **6**, 511–512 (2009).